Mon. Not. R. Astron. Soc. **371,** 380–394 (2006) doi:10.1111/j.1365-2966.2006.10666.x

# New techniques for integral field spectroscopy – I. Design, construction and testing of the GNIRS IFU

J. R. Allington-Smith,[1⋆] R. Content[1] C. M. Dubbeldam[2] D. J. Robertson[2] and W. Preuss[3]

[1]*Centre for Advanced Instrumentation, Durham University, South Rd, Durham DH1 3LE*
[2]*Centre for Advanced Instrumentation, Durham University, NetPark Research Institute, Sedgefield TS21 3FB*
[3]*Labor fur Mikrozerspanung, University of Bremen, Germany*

Accepted 2006 June 7. Received 2006 June 1; in original form 2005 November 22



**ABSTRACT**

We describe the integral field spectroscopy (IFS) capability of the Gemini Near-infrared Spectrograph (GNIRS) installed on the Gemini-South telescope. This makes use of the Advanced Image Slicer (AIS) optical concept of Content. Image slicing is, in principle, the most efficient technique of IFS. Our design is more compact and adaptable than the previous designs of this type so that the spectrograph can be switched to IFS mode simply by insertion of the integral field unit (IFU) into the focal plane. The near-optimal performance of the system makes it a good choice for instrumentation for future observatories, especially for the multiple-IFS systems required for extremely large telescopes (ELTs).

The IFU produces good image quality and high throughput (>90 per cent at wavelengths $\geqslant$2.5 μm) which can actually exceed that of a spectrograph with a conventional slit of the same width, due to the use of anamorphism that reduces losses due to diffraction. This also results in a square spatial sampling element (spaxel) while simultaneously providing Nyquist sampling of the slit. At short wavelengths, the throughput is determined by the quality of the finish of the optical surfaces but exceeds 60 per cent at 1 μm.

The three multifaceted mirror arrays in the slicing unit were made as monolithic units to avoid alignment errors between slices. This required the development of new freeform diamond-machining techniques which we describe. We present results on the testing of the optical components, and system-level tests to verify performance. We show that the IFU performs better than our expectations in terms of image quality and scattered light and that our model of the throughput, when fed with the results of our metrology of the surface quality, gives an accurate description of the performance measured in the laboratory.

Paper 2 gives the results of on-sky testing to confirm the results of the laboratory tests and to verify performance by reference to existing data sets obtained with conventional techniques. The verification of our performance model is of great importance to the planning of future instrumentation of this type, as is the 'plug-and-play' nature of the integration with the spectrograph. Further details of the optical design and the optimization process are given in Paper 3.

**Key words:** instrumentation: spectrographs – techniques: spectroscopic.

## 1 INTRODUCTION

Integral field spectroscopy (IFS) produces a spectrum for each spatial element (spaxel) in the field of view, allowing detailed studies of extended objects without the sampling errors, biases and inefficiencies inherent in slit spectroscopy. This technique has increased in importance as the use of large telescope apertures allows high signal-to-noise ratios to be obtained despite the division of the integrated light from discrete sources in both the spectral and (two-dimensional) spatial domains. Thus spatially resolved spectroscopy can be attempted even for faint, distant objects (e.g. Eisenhauer et al. 2004; Bower et al. 2004). Improvements in image quality through adaptive optics (AO) also increase the relevance of IFS by

⋆E-mail: j.r.allington-smith@durham.ac.uk

allowing dissection of nearby archetypical objects such as NGC 1068 (e.g. Gerssen et al. 2006) and by allowing the effective use of IFS on extremely large telescopes (ELTs). For example, IFS near the diffraction limit is a key technique for the study of intermediate black holes in dense star clusters and in resolving stars in extragalactic systems where the combination of spectral and spatial information helps overcome confusion. It can also be combined with multiobject spectroscopic techniques for IFS within observer-selectable fields within the corrected field of the telescope (e.g. Pasquini et al. 2000; Sharples et al. 2004). Many of the instruments proposed for ELTs are predicated on multiplexed IFS in combination with AO using multiobject or tomographic techniques facilitated by multiple laser guide stars. Thus, the development of highly efficient designs for IFS is central to the exploitation of the $\leqslant$50 m aperture telescopes currently being studied. Our aim in this paper is to demonstrate a design which, with modest improvement in manufacturing technology, will deliver near-optimal performance on ELTs.

The Gemini Near-Infrared Spectrograph (GNIRS) is a facility instrument on the Gemini-South telescope, designed for low and medium spectral resolution slit spectroscopy at wavelengths 1–5 μm. For optimum performance, it is cryogenically cooled with the entire optical system inside a large cryostat. This versatile instrument, built by the National Optical Astronomy Observatories of the USA (NOAO), was commissioned on the telescope in late 2003. The Gemini Observatory contracted Durham University to provide an integral field unit (IFU) for it. This is a small module which is installed in the slit slide (inside the cryostat) allowing it to be inserted into the beam remotely. The IFU reformats light from a field of 5 × 3 arcsec$^2$ into a pseudo-slit which is dispersed by the spectrograph in the same way as a normal long slit directly sampling the sky. The IFU was integrated into GNIRS at the telescope in early 2004 and commissioned later in the spring with excellent results, confirmed by subsequent system verification observations. GNIRS and its IFU are now in routine operation on Gemini-S. Its main features are summarized in Table 1.

In this paper, we describe the IFU, its design and the new methods used to make it and show results of tests in the laboratory at component and system level to verify conformity with the astrophysical requirements described in Section 2. Section 3 contains descriptions of the design of the optical system and mechanical structure. Section 4 describes how the optics were made and Section 5 gives the results of tests on these components. The closely coupled activities of integration, alignment and system-level testing are described in Section 6 which contains performance predictions which were verified later at the telescope. Section 7 contains our conclusions regarding the work reported so far and explains in more detail the relevance of this work to future instrumentation.

In Paper 2 (Allington-Smith et al., in preparation), we describe the integration of the IFU with the spectrograph and give results obtained at the telescope on the performance (image quality, throughput, uniformity of response, geometric properties, stability, straylight, etc.) and show example data sets and compare them with data from other sources to provide astrophysical verification of the performance. Paper 2 includes a critical assessment of the design, and the production methods used to realize it, in the context of the enormous challenges posed by ELTs. Paper 3 (Content, in preparation) provides further detail of the Advanced Image Slicer (AIS) design concept and its application to GNIRS.

**Table 1.** Summary of GNIRS IFU.

| | On sky (arcsec) | On detector (pixels) | Physical (mm) |
|---|---|---|---|
| Spatial sampling | 0.15 × 0.15 | 1 × 2 | (0.34 × 0.79 at S1) |
| Field of view | 4.8 × 3.2 | | 10.9 × 16.5 at S1 |
| Slice dimensions | 4.8 × 0.15 | 32.3 × 2.0 | 10.9 × 0.79 at S1 |
| Pseudo-slit dimensions | (120) | 798 × 2.0 | 73.0 × 0.09 at S3 |
| Number of slices | | 21 | |
| IFU pre-magnification | | 3.7 × 8.5 | |

## 2 REQUIREMENTS

The basic requirement placed on the IFU was to sample a field of view of several arcsec on a side at the resolution allowed by the number of illuminated detector pixels. The field size was driven by astrophysical considerations using the example of optical/radio coaligned radio galaxies which have extended line emission on scales up to 5 arcsec, but rarely larger, and by the operational constraint that target acquisition is made easier if the field is large enough to acquire a point source by blind-pointing of the telescope, which requires a field of $\geqslant$3 arcsec. This implies a field area of 15 arcsec$^2$ with aspect ratio 1–1.5. The detector format of GNIRS is 1024 × 1024, but internal baffling in the spectrograph restricts the unvignetted portion to ∼700 pixels in the spatial direction when using the short camera. Thus the sampling increment on the sky, if square, would be roughly $\sqrt{15/700} = 0.15$ arcsec. This was considered to be consistent with both the expected image quality in the *K*-band with active optics and achievable signal/noise for faint extended objects such as the radio galaxies discussed above. Coincidentally, 0.15 arcsec is the sampling increment provided by the GNIRS short camera in direct imaging and slit spectroscopy modes. A field aspect ratio of 1.5 was adopted to optimize for non-spherical objects viewed in projection.

A further constraint was that the IFU's pseudo-slit has to be sampled by two detector pixels to conform to the Nyquist sampling theorem. During the development of the AIS concept, it was realized that, by using anamorphic techniques, the spaxels could be made square (projected on the sky) while still permitting Nyquist sampling of the slit by the detector. Since this would provide uniform sampling in orthogonal directions, making it easier to combine observations taken with different orientations, the feature was included in the instrument.

The engineering specifications were obtained by requiring that the image quality of the IFU should not degrade the image quality provided to the instrument, under Nyquist sampling conditions, by more than 10 per cent. The specification for throughput was taken as 70 per cent total for the IFU based on what was thought to be technically achievable. Additional specifications were adopted for scattered light based on the expected background signal from other sources and criteria adopted by other instruments. Further requirements were placed on stability during tracking to avoid degradation of the data during the course of a single exposure and to remove the need for frequent calibration which would reduce observing efficiency.

The biggest constraint on the design was the requirement that GNIRS converts to IFS mode simply by the remote insertion of a module fitted into the slit slide within the cryostat. The slide is a subassembly at the relayed telescope focal plane (after an Offner relay) which deploys slit and acquisition masks by moving the slide to fixed, repeatable positions in the dispersion direction. The IFU was required to occupy a position on the slit slide and so had to conform to a very precisely specified optical interface relating to

**Table 2.** Summary of requirements.

| | Requirement (goal) | Origin |
|---|---|---|
| Operational wavelengths | 1.0–2.5 (1–5) μm | Astrophysics/GNIRS |
| Field of view | 3.2 × 4.8 arcsec | Astrophysics/GNIRS/achievable |
| Spatial sampling | 0.15 × 0.15 arcsec | Astrophysics/GNIRS/achievable |
| Image quality[a] | $d_{50} < 0.14$, $d_{90} < 0.45$ arcsec | Internal |
| Optical efficiency[b] | >70 per cent | Internal |
| Uniformity of efficiency | rms <10 per cent over field | Internal |
| Scattered light | Diffuse: <50 per cent of background | Internal |
| | Ghost: <1 per cent of parent | Internal |
| Stability | Degradation of IQ due to flexure: <10 per cent | Internal |
| | Motion of slit image on detector: <0.1 pixels/10 mins | Internal |
| Mass | <1 kg | GNIRS |
| Size | 200 × 100 × 100 mm$^3$ | GNIRS |
| Operating temperature | 60 K | GNIRS |
| Operating pressure | $10^{-4}$ Pa | GNIRS |

[a] $d_Q$ is the diameter of a circle enclosing $Q$ per cent of the energy in the PSF. This metric is only indicative because it does not fully account for the anamorphism of the optics; [b] from input to output including vignetting by spectrograph stop.

the location of the input and output focal surfaces and on the total mass and size.

The resulting specifications are summarized in Table 2 with the origin of the specification indicated. *GNIRS* means set by the capabilities of the spectrograph; *internal* means set by the GNIRS IFU team as required to provide acceptable performance while reaching the top-level goals; *achievable* indicates practical solutions constrained by the other factors involved.

## 3 DESIGN

### 3.1 Advantages of image slicing for IFS

The general background to IFS is summarized in Allington-Smith & Content (1998); which also discusses sampling and background subtraction issues relevant to fibre-lenslet IFS. As shown in Allington-Smith (2006), the most general figure of merit is the specific information density (SID):

$$Q = \eta \frac{N_p N_q N_\lambda}{N_x N_y}, \quad (1)$$

where $N_p$ and $N_q$ are the numbers of spatial resolution elements in orthogonal directions $p$ and $q$ in the field. These quantities are related to the numbers of spaxels via $N'_p = N_p f_s$, $N'_q = N_q f_s$ where $f_s$ is the oversampling of the point spread function (PSF) by the *IFU*, normally chosen as $f_s = 2$. $N_\lambda$ is the number of spectral resolution elements related to the number of spectral samples by $N'_\lambda = N_\lambda f_\lambda$ where $f_\lambda$ is the spectral oversampling by the *detector*. $N_x$ and $N_y$ are the numbers of pixels in the detector in orthogonal directions $x$ and $y$ and $\eta$ is the throughput of the IFU.[1] $x$ and $y$ are aligned with directions $p$ and $q$ on the sky in the sense that $p$ is the dimension that varies most rapidly along the slit which is defined by the detector $y$ direction. The theoretical maximum SID is obtained when $N'_p N'_q N'_\lambda = N_x N_y$, for Nyquist sampling ($f_s = f_\lambda = 2$) and $\eta = 1$ as $Q_{max} = 1/8$.

[1]Measured from the IFU's input to its output but including losses at the spectrograph stop, or, by comparison with the same spectrograph using a single slit of the same equivalent width.

Although this is a useful figure of merit for comparing different IFS systems, a comparison of different '3D' techniques including those such as Fourier transform spectroscopy, which use a number of separate exposures to generate the spectral information, requires a more general metric such as $Q/n_e t_e$ where $n_e$ is the number of separate exposures and $t_e$ is the duration of each.

It should be noted, that SID is a measure of the information obtainable per detector pixel but does not take into account the quality of the data actually obtained. For that, the figure of merit must be based on signal/noise considerations which are dependent on the particular astrophysical investigation in question.

Using SID as a figure of merit, image slicers score higher than other techniques ($Q/Q_{max} \simeq 0.7$ for the GNIRS IFU) because the pitch between spaxels along the slit is effectively one detector pixel, whereas the spacing with lenslet arrays (Bacon et al. 2001[2]) and lenslet-coupled fibre array systems is much larger (e.g. five to six for the GMOS – Allington-Smith et al. 2002 – and VIMOS – LeFevre et al. 2003 – IFUs). Image slicer designs are relatively easy to implement in cooled instruments since the optical surfaces can be made from the same material as the support structure to eliminate differential thermal expansion so that the optical elements remain aligned at all temperatures.

### 3.2 Advanced Image Slicer

The optical design is based on the *AIS* paradigm (Content 1997, Paper 3) illustrated in Fig. 1. It differs from the earlier 3D concept (Weitzel et al. 1996) in that each mirror facet is curved rather than flat. This means that the slicing mirrors (S1) located at a conjugate of the sky not only divide the image into one-dimensional pieces but also form images of the telescope exit pupil on an array of pupil mirrors (S2), one for each slice. This allows the tilt angle of the slicing mirrors to be minimized since the S2 mirrors do not need oversizing which helps to reduce aberrations and make the system small. The pupil mirrors are also curved so that they form images of the sky on a matching set of mirrors (S3) located at the input focal

[2]However, Keck OSIRIS achieves a significantly larger SID than previous devices of this type (Larkin et al. 2006).

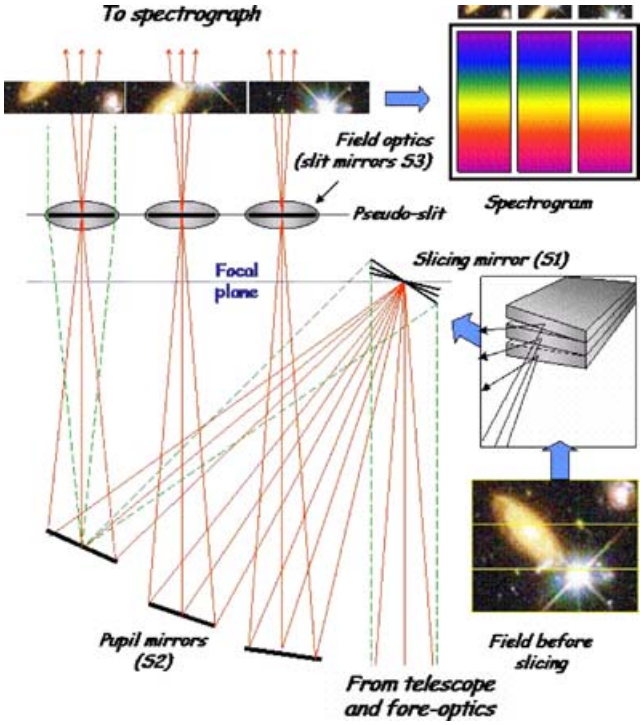


**Figure 1.** An illustration of the principle of the *AIS* equipped with three slices for simplicity and ignoring the foreoptics.

surface of the spectrograph. These are arranged end to end to form a pseudo-slit, thus effecting the two- to one-dimensional reformatting of the field. Finally, the S3 mirrors are also curved to re-image the pupil on to the spectrograph stop. Details of the operational principle and its application to a number of specific instrument designs may be found in Paper 3. Here, we give a summary of the main features of the design principle and those details which are directly relevant to the GNIRS IFU.

### 3.3 Optical layout

The optical layout of the IFU is shown in Fig. 2. It is very compact: the whole unit had to fit within an envelope of $0.1 \times 0.2 \times 0.1$ m$^3$ and mass limit of 1 kg. It includes foreoptics to pre-magnify the sky image to match the physical slice width which is practically achievable (790 μm) compared to that of the original *f*/16 focus of the telescope (93 μm). The IFU is located behind the foreoptics of GNIRS which contains an Offner relay giving unit magnification. The foreoptics of the IFU consists of three unsegmented mirrors comprising a flat pickoff located at the sky conjugate and two off-axis aspheric mirrors.

The foreoptics not only provides the required magnification but also anamorphically magnifies the sky image by an extra factor of 2.3 in the dispersion direction. This means that the slit width, defined by the slice width of 0.15 arcsec, is sampled by two detector pixels when the light is dispersed, assuming a typical anamorphic factor of 1.15 for the spectrograph due to the non-Littrow mounting of the disperser. Without dispersion, the pseudo-slit width projects to 2.3 pixels. However, the same spatial extent on the sky along the slit is sampled by only one detector pixel. This allows for a regular square sampling pattern while simultaneously giving Nyquist sampling of the spectral resolution element and making maximum use of the detector surface (Fig. 3).

A further advantage of this approach is that the output beam underfills the spectrograph stop in the dispersion direction by a factor of 2.3 which reduces losses due to diffraction which broadens the beam in the same direction (see Fig. 3). This means that, when compared to the same spectrograph in slit spectroscopy mode, diffraction losses will be smaller and hence, in principle – at long wavelength when using narrow slits – that the throughput of the IFU could actually exceed that of the spectrograph alone. We will show in Paper 2 that this actually happens. In terms of information theory, the penalty of playing these tricks to enhance performance is that the spectral resolution obtained is that appropriate to a slit width of 0.35 arcsec, not 0.15 arcsec.

In order to simplify manufacture, all mirrors have a spherical figure with a common radius of curvature within a single mirror group except for the S3 mirrors which are toroidal and have different curvatures in the spatial direction. This results in a small variation in image scale between the centre and edges of the slit (Fig. 4). Further details are given in Paper 3.

The input focal surface of the IFU coincides with the output of the spectrograph's foreoptics. The IFU's input and output optical axes are parallel to that of the spectrograph as defined at the slit centre and the input field is displaced by 6.0 mm in *y* from the centre of

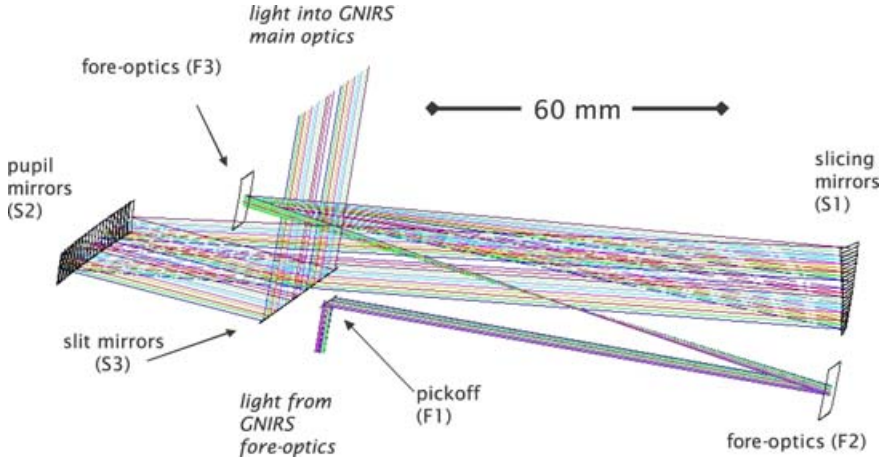


**Figure 2.** Layout of the optical system of the IFU with the foreoptics elements (F*n*) and slicing optics (S*n*) labelled. For simplicity, only one ray is shown for each of the 21 optical paths. Conjugates of the sky are located at F1, S1 and S3 and conjugates of the exit pupil of the telescope are located at S2 and at the spectrograph stop (not shown).

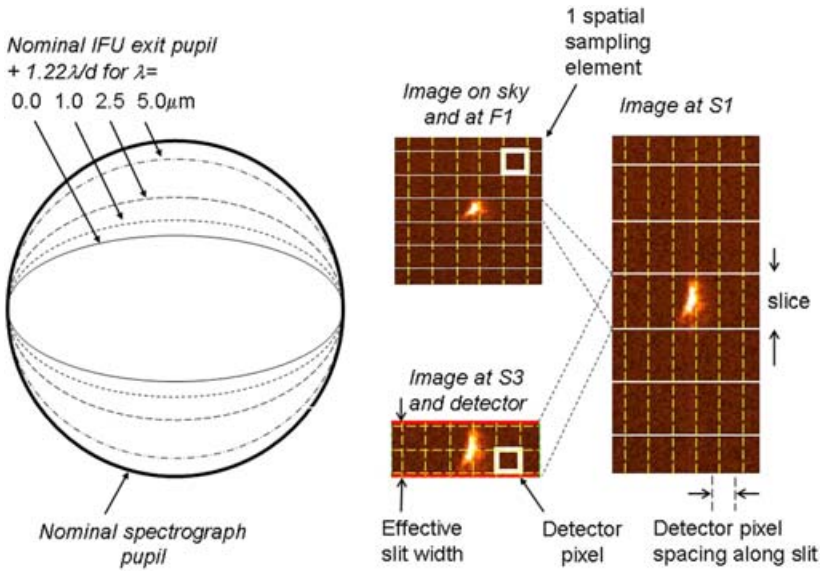


**Figure 3.** Illustration of the effects of the anamorphic magnification described in the text. Left-hand image: the effect on the exit pupil and its match to the nominal spectrograph stop. The actual stop is slightly oversized and has a more complicated shape than shown. The effect of diffraction in the dispersion direction is shown schematically by adding the size of the diffracted beam (to the first null) at the wavelengths, λ, shown. Right-hand image: the effect on the image shown at sky conjugates, at S1 after anamorphic magnification by the foreoptics and at the pseudo-slit, S3. The detector grid and its projection along the slit is indicated by dashed lines while solid lines indicate the slice boundaries. The spatial sampling element is thus defined by the detector grid spacing in the spatial direction and by the slice width in the dispersion direction. Although the sampling element projected on the sky is conveniently square, the slice width is sampled by two detector pixels for proper Nyquist sampling (once the additional anamorphism due to the spectrograph is accounted for). The image shown as an example is one of those recorded during system image quality tests, as described below.

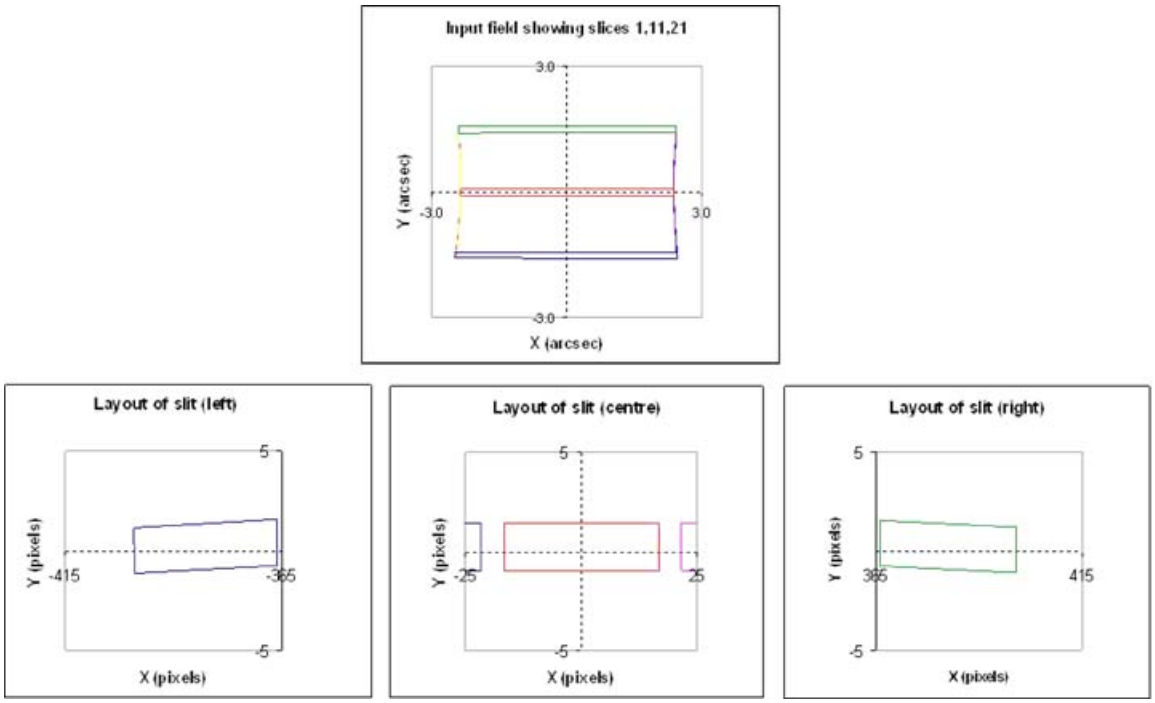


**Figure 4.** Top panel: predicted layout of input field showing the small variation in image scale evidenced by the curvature of the edge of the field. Bottom panel: layout of the pseudo-slit showing slices 1, 11 and 21. To show the slight rotation of the outermost slices, the vertical scale has been exaggerated by a factor of 5.

the GNIRS field. The IFU is designed so that the images of the slit mirror exit pupils are superimposed on the spectrograph stop.

The optical system was arranged to feed the spectrograph with the short camera deployed. The internal baffling of GNIRS was designed for a slit somewhat shorter than that of our original design of 21 slices. In order to maximize the field of view, we opted to retain the maximum slit length and to reduce the vignetting of the outer slices by judicious angling of the four outermost S3 mirrors

so that those slices would have significant throughput despite being outside the extent of the long slit.

### 3.4 Image quality predictions

The image quality was assessed by ray tracing. Straylight due to diffraction was accounted for separately as described below. The spot diagrams are pan-chromatic since there are no transmissive components. All the optical design work described here was done using ZEMAX.

We need to consider three assessments of the image quality as listed below.

(i) The image of a point source originating in the focal plane of the telescope formed by the IFU foreoptics on the slicing mirror. This demonstrates the ability of the IFU to accurately subdivide the input image in the dispersion direction.

(ii) The image of a point source on the slicing mirrors formed by the slicing optics at the pseudo-slit. This gives an estimate of the PSF in the spectrum.

(iii) The image of a point source originating in the focal plane of the telescope formed at the pseudo-slit after processing by the IFU. This gives an estimate of the PSF in the spatial direction along the slit and, in the dispersion direction, an estimate of the convolution of the component of the spatial PSF in the dispersion direction with the spectral PSF.

In practice, if the PSF on the S1 is much smaller than the slice width in the dispersion direction, then demonstrating (ii) will also demonstrate (iii).

Fig. 5 shows spot diagrams for images formed at S1, corresponding to assessment (i) over the full IFU field. This shows that the PSF is much smaller than the slice width so the IFU will accurately subdivide the field. Fig. 6 shows spot diagrams traced from S1 to S3 corresponding to assessment (ii), for the top, middle and bottom slices. The size of the boxes corresponds to 1 pixel on the detector. Even in the worst case, these PSFs have ∼100 per cent energy

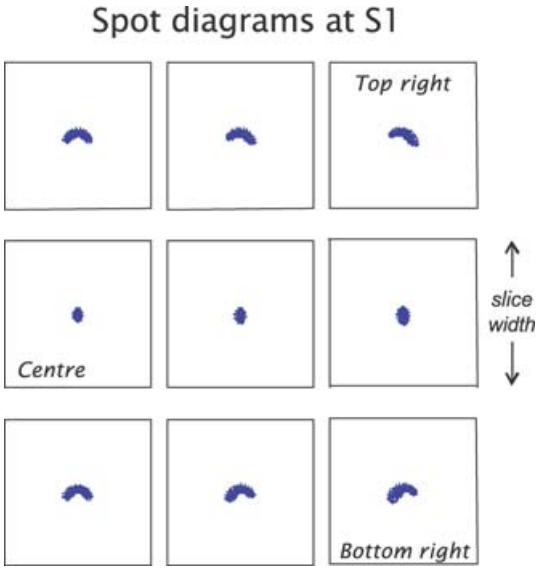


**Figure 5.** Spot diagrams at S1, the conjugate of the sky where the slicing is performed, showing rays traced through the telescope and IFU foreoptics. Half of the field is represented, the centre being the middle-left box while the top-right and bottom-right boxes correspond to the corners of the field. The size of each box is equivalent to the slice width.

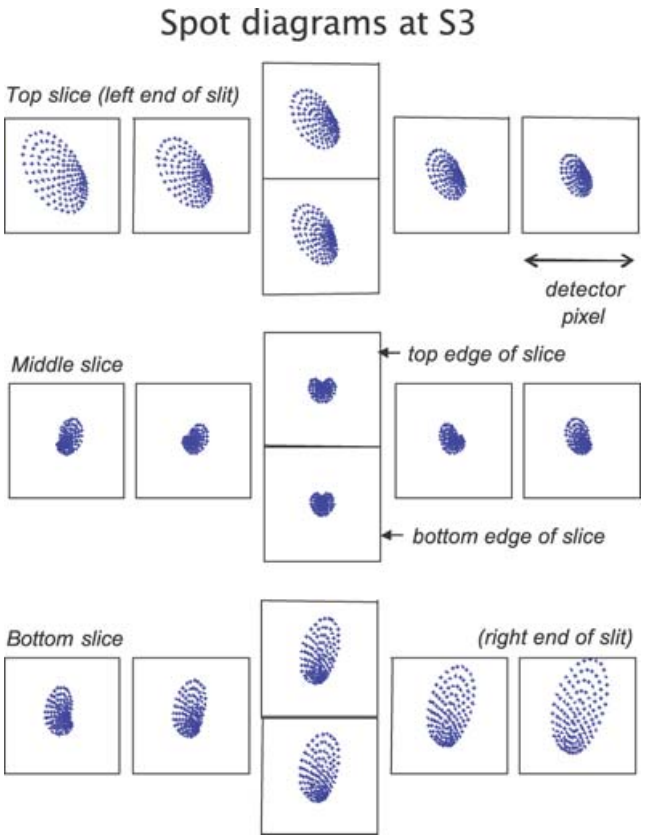


**Figure 6.** Spot diagrams at S3 due to point sources at various locations in the image conjugate of the field at S1. The three lines of plots are for slices 1, 11 and 21 at locations along the centreline of the slices, apart from the plots in the centre which refer to the top and bottom edges of the slice. The size of the box corresponds to one detector pixel.

contained in one pixel. This is better than the specification of $d_{50} = 0.93$ pixel. However, remember that the PSFs given in these figures do not include the effect of diffraction.

Diffraction by S1 was simulated by splitting each ray hitting S1 into seven rays that follow the distribution of diffracted light in the dispersion direction. Further details are given in Paper 3. The rms image size was calculated in the merit function used to optimize the optical design. The difference in the design when optimized with and without diffraction is very small. The same is true for the image size, which is only increased by a few per cent. The average image size at the slit when diffraction is included in this way is $d_{50} = 12\,\mu$m (13 per cent of the slit width or equivalent to 0.04 arcsec) compared with the specification, assuming the PSF on the sky is Gaussian of $d_{50} = 52\,\mu$m. Thus, the design conforms to the specification for image quality with a large contingency to account for errors in manufacture and alignment.

### 3.5 Baffles

Since some scattering of the incident light was expected, it was necessary to consider how this could be prevented from reaching the detector where it might degrade the image quality, produce discrete or unfocused ghosts or cause cross-talk between slices.

Scattering from the S1 mirrors would result in light missing the nominal pupil and being vignetted at the spectrograph stop even if it had been not already rejected by the S2 mirror apertures which

act as slightly oversized pupil stops. The same argument applies to S3 which is at a conjugate of S1. Light scattering from the S2 mirrors has the potential to produce artefacts in the image plane but is reduced by the restricted aperture of the S3 mirrors which act as field stops.

However, light scattering from S1 has the potential to strike the wrong S2 mirror resulting in a ghost image appearing in a slice adjacent to the one in which the point source is placed. Since, as discussed later, the scattering is isotropic, we can estimate the fraction of the incident light which is scattered (using the formula for total integrated scattered light, Section 4.2) into the solid angle subtended by an adjacent S2 mirror [$\sim(d_2/L_{12})^2/4\pi$, where $d_2$ is the aperture of each S2 facet and $L_{12}$ is the separation between S1 and S2]. At the shortest wavelength of $\lambda = 1$ μm, taking the worst-case roughness of $\sigma = 20$ nm (Section 5.3) and $d_2 = 5$mm, $L_{12} = 130$ mm the fraction is $\sim 10^{-5}$ so we expect this effect to be negligible. See Paper 3 for a full discussion.

Instead of making detailed numerical simulations of scattered light, we decided to use our limited resources to design a set of baffles filling the interior of the IFU and adjust them as necessary. This consists of sheets of opaque, infrared-absorbing material with clear apertures tailored to the permitted ray paths.

### 3.6 Mechanical design of support structure

The IFU's optomechanical design was driven by the following considerations.

(i) For operation at infrared wavelengths, the IFU must be cryogenically cooled. This requires that all components are sufficiently robust to endure cold operation and thermal cycling, and that the performance of the IFU is predictable and maintainable at cryogenic temperatures. In order to eliminate effects of differential thermal expansion and thus ensure compatibility with the cryogenic environment, all components (including the optical components) are made from aluminium.

(ii) The IFU must fit inside a space envelope of 200 × 100 × 100 mm$^3$ and have a mass of 1.0 kg. A major constraint on the design is the presence of the decker slide, which restricts the space immediately in front of the slit slide, and thus limits the possible positions of the optical elements.

The IFU contains 66 individual optical surfaces. In order to maximize system performance, the demands on the quality and alignment accuracy of the optical components are very high. Very smooth optics are required to minimize scattered light, which would otherwise increase the background. The limitations on the available space envelope make it impractical to align each optical surface individually. Although it is possible to assemble them into arrays which can be pre-aligned before system integration, we could not do this with sufficient accuracy. The main problem is the S1 mirrors since we could not make the blanks of these high-aspect mirrors sufficiently flat to permit accurate alignment. These considerations drove us towards the implementation of diamond-machined monoliths for the S1, S2 and S3 arrays. It is then no longer necessary to align individual mirrors, thus simplifying the integration and subsequent testing of the IFU. We therefore developed a technique for the fabrication of monolithic multifaceted mirror arrays using freeform diamond machining as described in Section 4.3.

We exploit the inherent accuracy of the diamond machining equipment to provide the required relative alignment accuracy of the facets, as well as the required optical surface quality. Datum surfaces were machined in the same operation where possible, in order to further enhance the accuracy. In addition, the consequential reduction of the errors in the relative alignment of optical surfaces within a monolithic array enables us to relax the tolerances on the absolute alignment of an array. This contributes further to the ease of integration and test. A number of critical reference and mounting surfaces on the mounting brackets and IFU housing were also diamond machined to further enhance the alignment accuracy. The design of the mounting components incorporates provisions for the alignment of the optical components in five degrees of freedom, thus facilitating the optimization of the IFU's optical performance and the accurate alignment of the input and output pupil. A three-point mount fixes the IFU inside the GNIRS slit slide mechanism; a reference (datum) edge defines the module's alignment about the optical axis. Although the IFU was designed to be installed without the need for alignment ('plug and play'), the unit can be aligned with respect to the instrument's optical axis through shimming. No adjustment of the internal components was to be made during installation and alignment of the IFU in GNIRS. Fig. 7 shows the mechanical support structure. See also Dubbeldam et al. (2004) for additional information.

## 4 FABRICATION OF THE OPTICAL SYSTEM

### 4.1 Tolerances on optical component geometry and surface form

The tolerances were calculated using the tolerance analysis capability of ZEMAX. We calculated the precision needed for each of 56 values in the design including de-centre, surface form, tilt, axial displacement, radius of curvature and axial rotation for the off-axis aspheric mirrors. Individual and global errors were considered as separate sources of error for the multifaceted mirror arrays. The errors were distributed so that the total error does not exceed the defined limit with a confidence interval of 98 per cent. The calculations were performed without adjustments as a worst case and to determine to what precision adjustments would need to be made. Further details are given in Paper 3.

Three merit functions were defined representing:(i) image position error in the output focal plane; (ii) image quality and (iii) loss of light by vignetting at the stop of the spectrograph.

The limit of acceptable image position error was fixed at 1 pixel. This is important to avoid vignetting at the slit and to avoid partial superposition of adjacent images. The image quality is determined by the specifications, $d_{50} \leqslant 0.93$ pixel. The vignetting merit function, (iii), is a combination of pupil image position error and pupil image quality. It also takes into account the anamorphic magnification of the pupil image which makes it much smaller than the stop in the dispersion direction, so the position error can be larger and the image quality can be worst in this direction.

The results are summarized in Table 3, which shows tolerances for both individual mirrors and complete subassemblies for displacements, $D$, and rotations, $R$, about the subscripted axis to be assessed by measurements on the location of the PSF.

The orthogonal coordinate frame used throughout this paper is local to the piece in question with $x$ along the length of the slice and $z$ along the local optical axis (not generally normal to the surface) so that $y$ is in the direction of dispersion.

### 4.2 Tolerance on surface roughness

The optical system of the IFU comprises 21 optical paths, each containing six reflecting surfaces, 66 in total. Each surface can scatter

**Table 3.** Summary of requirements resulting from tolerance analysis.

| Optical component | Translation (μm) | | | Rotation (μrad) | | | Surface form[b] | Radius of curvature[ab] |
|---|---|---|---|---|---|---|---|---|
| | $D_x$ (μm) | $D_y$ (μm) | $D_z$ (μm) | $R_x$ (μrad) | $R_y$ (μrad) | $R_z$ (μrad) | ($/\lambda_e$) | ($/\lambda_e$) |
| F1 | | | 10 | 290 | 290 | | 0.24 | (Flat) |
| F2 | 10 | 10 | 20 | 200 | 200 | 3500 | 0.24 | (Asphere) |
| F3 | 20 | 16 | 20 | 200 | 200 | 1750 | 0.24 | (Asphere) |
| S1 (individual) | 12 | 20 | 20 | 290 | 290 | 1750 | | 0.8 |
| S1 (assembly) | 17 | 18 | 20 | 290 | 290 | 1750 | | |
| S2 (individual) | 10 | 10 | 20 | 200 | 200 | 220 | 0.24 | 2.0 |
| S2 (assembly) | 10 | 10 | 20 | 200 | 200 | 220 | | |
| S3 (individual) | 20 | 20 | 10 | 290 | 290 | 3500 | | 1.3 |
| S3 (assembly) | 20 | 20 | 10 | 290 | 200 | 290 | | |

[a]Surface form due to the radius of curvature error; [b]peak to valley; evaluation wavelength is $\lambda_e$ = 633 nm.

light that will reduce the throughput of the optical system since it is designed to stop straylight reaching the detector by blocking it with baffles inside the IFU or within the spectrograph, chiefly at the stop. The total fraction of scattered light from each surface may be estimated as:

$$S = \left(\frac{4\pi\sigma}{\lambda}\right)^2,$$

where $\sigma$ is the rms surface roughness and $\lambda$ is the wavelength. On this basis, a simple model of the throughput was devised using the measured rms surface roughness of each mirror facet in S1, S2, S3 and of the foreoptics mirrors. From this, the total throughput was calculated for the $j$th optical train defined by the unique series of facets in S1–S3 along which the rays propagate.

$$\eta_j(\lambda) = \prod_{k=1,6} R_k(\lambda)\left[1 - \left(\frac{4\pi\sigma_{jk}}{\lambda}\right)^2\right],$$

where $\sigma_{jk}$ is the measured rms surface roughness of facet $j$ for the $k$th mirror in the optical train (F1–F3, S1–S3) and $R_k$ is the surface reflectivity of the $k$th surface. Since the surface roughness varies from facet to facet, some overall variation of throughput with facet index $j$ is expected. The tolerance on this is related to the specified 'uniformity of efficiency: rms <10 per cent over field' entry in Table 2.

Assuming a gold coating with $R_k = 0.985$, independent of $\lambda$, and that all $\sigma_{jk}$ are the same, this suggests that we need $\sigma = 10$ nm to obtain 90 per cent throughput at the most demanding wavelength, $\lambda = 1$ μm due to this source of loss. The error budget for total throughput, 70 per cent, included an allocation of 90 per cent for surface roughness effects, and early prototypes had suggested that $\sigma = 11$ nm was possible, so we set the tolerance on the surface roughness to $\simeq$10 nm. This is a very simple estimate since it assumes that the multifaceted mirrors comprising S1–S3 achieve the same finish as the single larger mirrors which comprise F1–F3, whereas the latter are likely to be easier to manufacture. The total internal scatter assumption is also simplistic. The model also neglects diffraction loss on the grounds that this has only a small effect at the shortest wavelength of operation where scattering losses are likely to dominate. Nevertheless this model gave a useful estimate of the tolerance required to realize our throughput requirement. It turned out that it gives a prediction of the throughput as a function of wavelength that is very accurate when real measurements of $\sigma_{jk}$ from surface metrology are used.

### 4.3 Fabrication of monolithic mirror arrays

Although diamond-turning technology is not new, the techniques required to accurately fabricate metal monolithic mirror arrays with the complex geometry specified for the GNIRS IFU (where the spherical or toroidal facets have different orientations, and possibly different radii of curvature) have only recently become available. On a conventional diamond-turning lathe, the optical component is mounted on a spindle and the diamond tool follows an arbitrary path in the $x$–$z$ plane (where $z$ is parallel to the spindle axis) using high-precision translation stages. So, while the work piece is spinning, the tool is used to generate a rotation-symmetric optical surface, e.g. a flat, sphere, or a rotation-symmetric asphere. This technique was used to fabricate the F2 and F3 mirrors.

As described in Section 3.6, it was necessary to machine the mirror arrays as monoliths in order to exploit the inherent accuracy of the diamond-machining equipment. This required the addition of a translation stage to move the component in the vertical, $y$, direction and an additional rotation stage on which a tool-holding spindle is mounted. The diamond-turning machine is thus converted to a fly cutter in which the work piece is not translated (Fig. 8).

The offsets required to give the optical surfaces their correct tip-tilt angles can then be obtained by translating the array using the machine's translation stages, without the need to re-position the work piece on the tooling plate prior to the fabrication of each subsequent facet. The accuracy is now determined by the inherent accuracy of the diamond- machining equipment. This allows us to obtain the required relative alignment accuracy of the facets, as well as providing a very good optical form accuracy on each facet.

With this approach, it is possible to produce optical surfaces with a variety of surface geometries (Fig. 9). The monolithic S1–S3 arrays were fabricated using the freeform diamond-machining technique illustrated in the lower panel. This technique also makes it possible to machine reference surfaces integral to the arrays to a very high precision, thus enhancing further the accuracy and simplifying the IFU's integration and alignment. See Dubbeldam et al. (2004) for further details.

The S1–S3 arrays were machined from either single pieces of aluminium (S2, S3) or two pieces of aluminium in the case of S1 (the two subarrays are designated S1-A and S1-B). To reduce the problem of surface errors at the junction between adjacent surfaces, the optical design was modified to increase the dead space between the facets in the S2 and S3 arrays. This took the form of deep cuts in the blanks which served as an effective baffle between adjacent

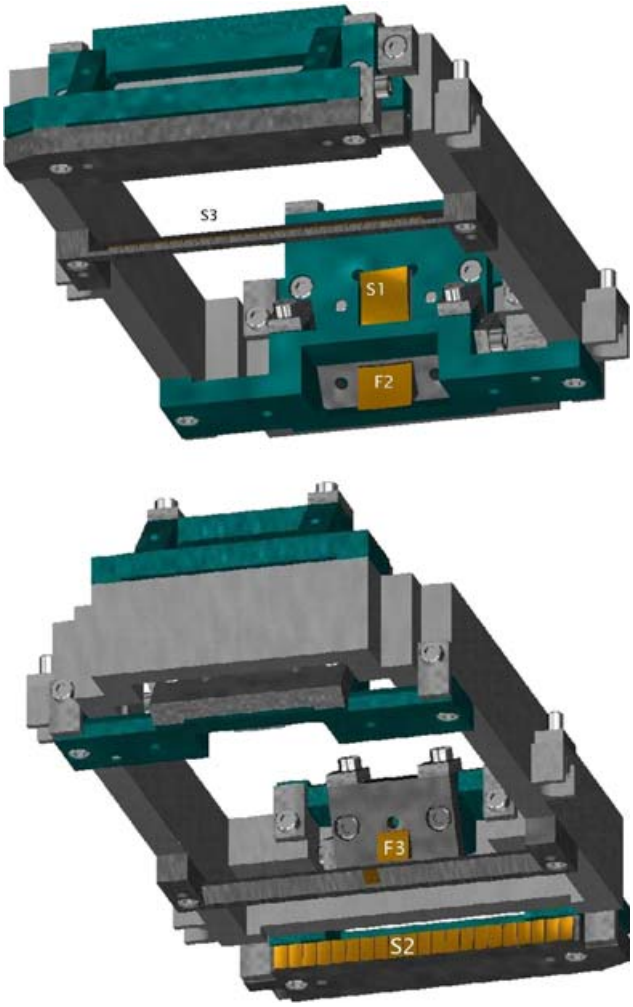


**Figure 7.** Mechanical structure showing the support structure and mounting assemblies of the mirrors (marked).

facets to further reduce scattered light (see above) at the expense of an increase in the length of the pseudo-slit and attendant vignetting loss at the extreme ends. This approach could not be used for the S1 array which is required to segment the field with high filling factor. Instead the machining process was optimized to minimize rounding and edge defects between slices. To reduce the step height between adjacent slices the S1 array was made in two halves to be mated during assembly.

Each mirror assembly was made with three integral mounting points with shimmable interfaces to the main structure of the IFU. This allowed the piece to be aligned in those three of the six possible degrees of freedom which were most critical via optical tests using temporary shims which, after the alignment was complete and all tests done, be turned into permanent alignments by machining the interface surfaces (to 1-μm accuracy).

Finally, after component-level testing to verify performance, the mirror arrays were coated with gold and the non-optical surfaces adjacent to the optical surfaces blackened wherever possible using Nextel paint to suppress scattered light.

## 5 TESTING OF OPTICAL COMPONENTS

After completion of the fabrication process, the components were subjected to extensive acceptance tests, prior to system integration.

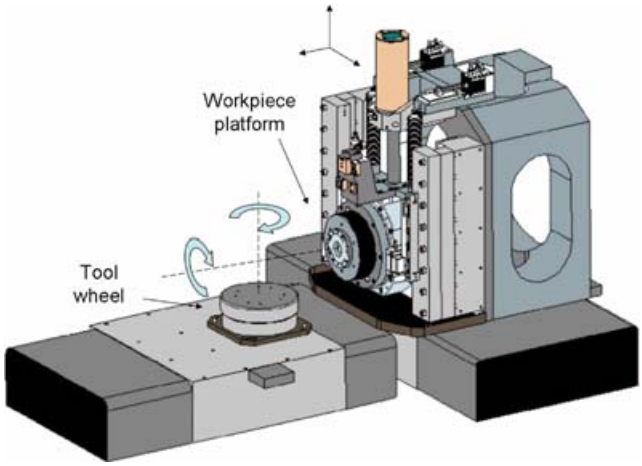


**Figure 8.** Illustration of the basic geometry of a fly cutter which provides five degrees of freedom (two rotations of the wheel on which the cutting tool is mounted and of the work-piece platforms – as marked – and three orthogonal translations of the work-piece platform) to generate a wide variety of shapes.

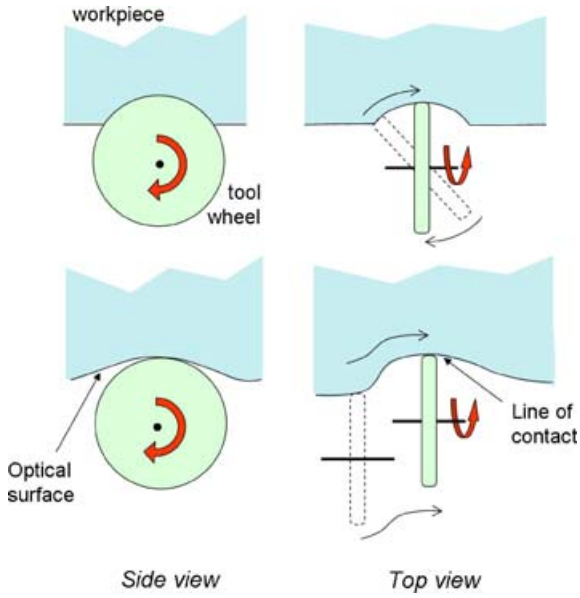


**Figure 9.** Illustration of techniques for generating optical surfaces by diamond machining using different numbers of degrees of freedom. Top image: production of a spherical surface by rotation only of the fly cutter about its centre point. The optical surface's radius of curvature is then identical to the radius of the fly cutter. The correct orientation of the optical surface can be obtained by offsetting the array relative to the fly cutter's centre point using the machine's horizontal ($x$) and vertical ($y$) translation stages. Bottom image: production of a freeform surface by choosing the fly cutter radius to be smaller than the local curvature of the optical surface. The cutter will be in contact with the surface at a discrete point only as the wheel is translated along adjacent tracks perpendicular to its plane. This enables one to fabricate optical surfaces with arbitrary geometries by a process similar to sculpture.

The objective of these tests was to verify their compliance with the following requirements.

(i) Geometry of the components, i.e. positioning and alignment accuracy (given by the location of the vertex and the orientation of the normal vector to it) and the curvature of the optical surfaces.

**Table 4.** Summary of component geometry measurements.

| Optical component | Translation (μm) | | | Rotation (μrad) | | | Surface form[bc] | Radius of curvature[abc] |
|---|---|---|---|---|---|---|---|---|
| | $D_x$ (μm) | $D_y$ (μm) | $D_z$ (μm) | $R_x$ (μrad) | $R_y$ (μrad) | $R_z$ (μrad) | (/$\lambda_e$) | (/$\lambda_e$) |
| F1 | | | **21** | **360** | **358** | | | |
| F2 | 0 | 0 | 7 | 161 | 43 | 53 | | |
| F3 | 10 | 0 | 15 | 8 | 0 | 10 | | |
| S1 (individual) | | | 1 | 44 | 38 | 4 | 0.09 | |
| S1 (assembly) | 1 | 0 | 18 | 10 | 33 | 123 | | |
| S2 (individual) | | | 1 | 125 | 205 | 13 | 0.15 | 0.26 |
| S2 (assembly) | 5 | **30** | **90** | **676** | **240** | 525 | | |
| S3 (individual) | | | | | | | 0.28 | 0.44 |
| S3 (assembly) | | | | | | | | |

*Notes*. Coordinate system is local to each surface. Values for facet-to-facet variations are the worst-case results. Evaluation wavelength is $\lambda_e$ =633 nm.
[a]Surface form due to the radius of curvature error; [b]peak to valley; [c]relative to nominal optical surface.

(ii) Form accuracy of the optical surfaces on scales $\geqslant$1 mm.
(iii) Roughness of the optical surfaces on scales $<$1 mm.

### 5.1 Component geometry

Errors in the component geometry, introduced during fabrication, are made up of the following.

(i) Set-up errors: global alignment errors relative to the datum surfaces which are common to all facets on the array. These errors can be corrected by aligning the optical components during IFU integration.
(ii) Facet-to-facet variations, which cannot be corrected by alignment of the optical components.

The component geometry was evaluated using a coordinate measuring machine with a resolution of 0.1 μm, and a measurement accuracy better than 0.5 μm and with a non-contact 3D profilometer, with a resolution of 10 nm. The results are shown in Table 4.

These results are upper limits since they are likely to be dominated by measurement uncertainties (see below), particularly given the small baseline over which the measurements have been conducted.

### 5.2 Surface form accuracy

The form accuracy of the optical surfaces (defined as the deviations from the theoretical optical surface, measured over a spatial frequency range from 0 to 1 mm$^{-1}$) was measured with an interferometer. We estimate the accuracy of the measurements to be 0.01 $\lambda_e$ rms ($\lambda_e = 633$ nm). The measurement results are summarized in the *surface form* and *radius of curvature* columns in Table 4. The results demonstrate the excellent surface quality that can be achieved with the freeform diamond-machining process.

### 5.3 Surface finish

The roughness of the optical surfaces (defined as the deviations from the theoretical optical surface measured over spatial frequencies $>1$ mm$^{-1}$) was measured using a white-light interferometer. The low-frequency components were removed using a high-pass fast Fourier transform filter with a cut-off frequency of 1 mm$^{-1}$. In order to cover a significant fraction of the total surface area, a number of measurements were conducted for each individual optical surface. The average surface roughness, $\overline{\sigma}$, for each optical surface was estimated as the rms of $n$ individual measurements, $\sigma_i$, at locations within the optical surface. This should be acceptable for those optical surfaces where the beam's footprint covers a significant portion of the optical surface (F2, F3, S2). For surfaces near an image conjugate (F1, S1, S3) where the beam's footprint is very small, the local surface roughness is expected to dominate, and the averaging process is likely to smooth out any effects from the local surface topology.

**Table 5.** Summary of surface roughness measurements (nm).

| Mirror | Average over surface | | |
|---|---|---|---|
| F1 | 15.9 | | |
| F2 | 14.1 | | |
| F3 | 18.7 | | |
| | Best | Mean | Worst |
| S1-A | 12.0 | 20.0 | 28.0 |
| S1-B | 17.0 | 23.3 | 32.2 |
| S2 | 9.5 | 14.5 | 24.7 |
| S3 | 14.5 | 19.0 | 23.8 |

The measurement results are summarized in Table 5. This shows that the roughness specification of 10 nm was not achieved. Nevertheless, predictions using the roughness obtained indicated an acceptable throughput. The variation in roughness from facet to facet for S1-A, S1-B, S2 and S3 is shown in Fig. 10 and the predicted throughput from end to end (F1–S3) due to surface roughness and surface reflectivity is shown in Fig. 11 at the extreme design wavelengths of 1.0 and 2.5 μm.

It can be seen that, as well as random variations from facet to facet, there are systematic variations along the arrays. These are likely to be due to wear of the tool as work progresses in sequence from one facet to another. The throughput predictions show that the random facet-to-facet variations have a greater influence on the uniformity of the throughput at shorter wavelengths as expected since scattering losses are greater at shorter wavelengths. At 1.0 μm, the scatter in throughput from facet to facet and from one end of the

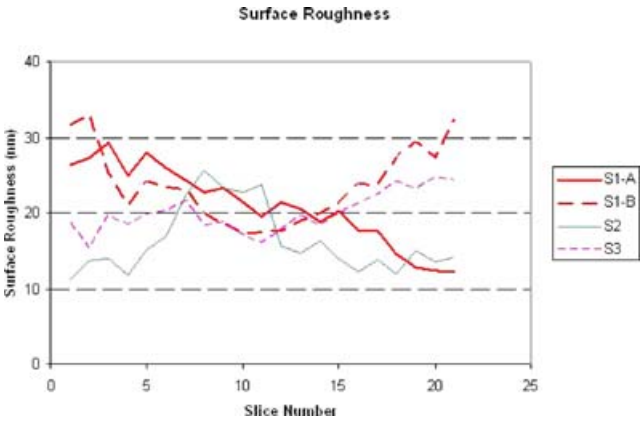


**Figure 10.** Roughness of each optical surface in the four monolithic mirror arrays (S1 is split into S1-A and S1-B) as defined in the text.

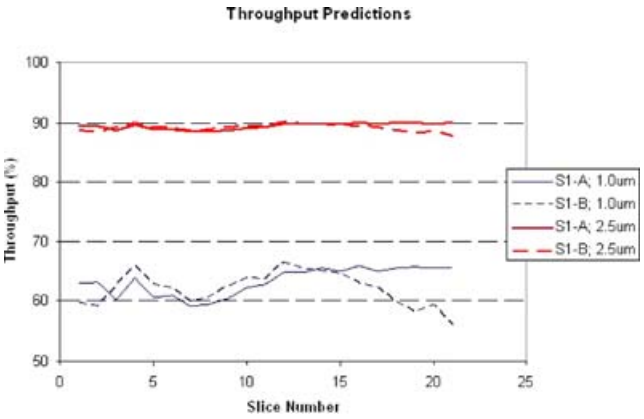


**Figure 11.** Throughput prediction for the optical train corresponding to each slice based on the simple model described in the text and our metrology of the optical surfaces. Results are shown separately for both halves of S1.

slice to the other is only a few per cent. The global throughput is predicted to be ∼63 per cent at the shortest operational wavelength which is close to our overall throughput specification (the model includes both surface scatter and the surface reflectivity, but excludes other effects). At longer wavelengths the throughput is predicted to be higher, reaching 90 per cent at the longest design wavelength (2.5 μm).

### 5.4 Effect of machining marks

Close inspection of the machined optical surfaces reveals periodic structures of low amplitude caused by the machining process (both the periodicity in the tool position and due to vibration of the work piece; Fig. 12). It was therefore necessary to consider if these structures act as diffraction gratings to scatter light in preferred directions where diffraction orders happen to coincide with the peak of a blaze function defined by the profile of the machining marks.

To test this, representative optical surfaces were illuminated with a collimated beam from an illuminated pinhole. The images formed by the converging beam from the curved mirror were re-imaged using a camera lens on to a CCD. Fig. 13 shows an image of the point source produced in this way for one case where discrete diffraction orders could be detected. This surface has a radius of curvature of

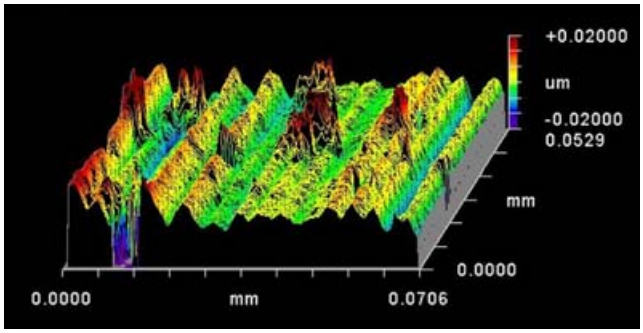


**Figure 12.** Isometric view of machining marks on a small portion of a mirror surface. The spherical surface has been subtracted. The spatial direction (along the slice) is parallel to the horizontal coordinate axis shown.

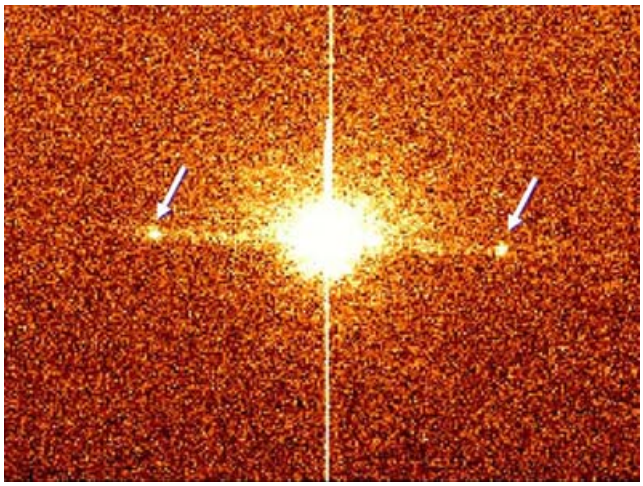

**Figure 13.** Images obtained as described in the text to search for anomalous effects due to machining marks acting as a diffraction grating. The saturated zero-order image of a pinhole is bracketed by two faint diffraction orders (arrowed) each containing 0.018 per cent of the light in the central peak. The vertical feature is a saturation artefact of the detector. The dispersion direction is approximately vertical on the plot. The area shown is 4 × 3 $mm^2$ at the focus of this spherical mirror (spatial × spectral directions; for comparison, the tested surface measures 3.3 × 6.0 $mm^2$).

66.2 mm. The surface form residual was measured as $0.3\lambda_e(P - V)$ and the roughness was 11-nm rms.

Analysis of the image showed that the two faint spots can be explained as the +1 and −1 diffraction orders for a grating with line spacing consistent with the measured periodicity of the machining marks on that piece. Because the intensity of each spot was only 0.018 per cent of the main image, we concluded that this was not a significant effect.

The fact that negligible energy is directed into the diffracted orders by this effect supports the assumption made above (Sections 3.5 and 5.4) that the scattered light is well represented by the total integrated scatter formula, which assumes isotropy.

### 5.5 Cryogenic test of gold coating

To check that the gold coating would perform well at cryogenic temperatures and survive temperature cycling without warping or delaminating, a witness piece (a rejected mirror array) was cooled slowly to ∼120 K by suspending it above liquid nitrogen, then

immersed in the cryogen and left for 1 h. After removal and unforced warming to room temperature, the witness piece was inspected. No defects were found.

## 6 INTEGRATION, ALIGNMENT AND TESTING OF OPTICAL SYSTEM

The assembly of the unit proceeded via a series of alignment checks. For this, an achromatic optical system was built to simulate illumination by a point source in an *f*/16 beam from the exit pupil of the telescope. This comprised a laser with a 10-μm pinhole acting as a spatial filter and a focal reducer to re-image the pinhole at the input focal surface of the IFU. After the IFU, another focal reducer re-imaged the pseudo-slit on to a CCD. The captured images analysed using the IRAF astronomical data reduction software package and IDL. Both the input and output stages were mounted on three-axis translation stages to allow the image quality and throughput at visible wavelengths to be studied over the complete field of the IFU and the complete length of the pseudo-slit, including the effect of focus changes.

The IFU was subjected to extensive system-level acceptance tests as follows.

(i) Image quality.
(ii) Output pupil alignment and dilation.
(iii) Scattered light and ghosting.
(iv) Throughput.
(v) A cold test was also carried out to demonstrate that the IFU meets all its performance requirements under cryogenic conditions.

### 6.1 Image quality

The IFU's image quality was assessed using the optical system described above. Examples of image quality data are shown in Fig. 14.

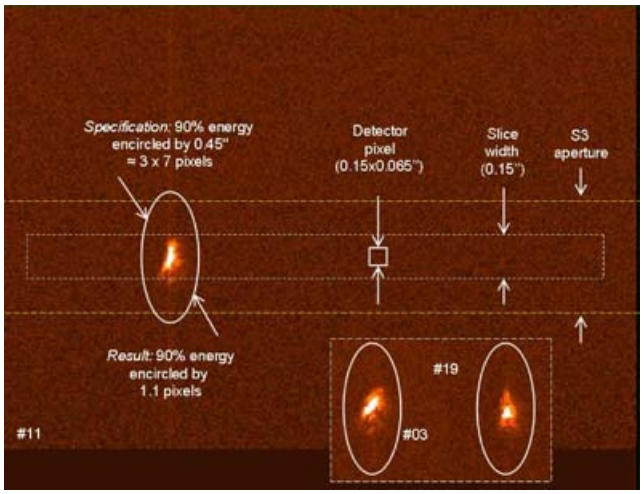


**Figure 14.** Image quality measurement at visible wavelengths during assembly and integration. This shows the image of a point source at a conjugate of the pseudo-slit for the central slice (number 11). For comparison, results from two other slices near the end of the pseudo-slit are also shown as insets. The measurement apertures are elliptical because of the anamorphism introduced by the IFU, as described in the text. The intensities are on a logarithmic scale to emphasize the wings of the PSF. The faint vertical streak is an artefact of the measuring apparatus (most likely the laboratory CCD). It also appears in calibration observations where the IFU is absent and extends – unphysically – beyond the extent of the S3 mirror.

**Table 6.** Summary of laboratory image quality measurements (arcsec on sky).

| | $d_{50}$ | $d_{90}$ |
|---|---|---|
| IFU – best | 0.054 | 0.151 |
| IFU – mean | 0.059 | 0.179 |
| IFU – worst | 0.063 | 0.207 |
| Requirement | 0.14 | 0.45 |
| Reference – no IFU | 0.031 | 0.098 |

Results of the measurement of image quality are summarized in Table 6.

The results demonstrate that the IFU produces excellent image quality, with $0.05 \leqslant d_{50} \leqslant 0.06$ and $0.15 \leqslant d_{90} \leqslant 0.21$ arcsec, respectively, compared to a top-level science requirement of $d_{50} = 0.14$ arcsec and $d_{90} = 0.45$ arcsec. The measurement results have not been deconvolved to separate the PSF produced by the IFU from the PSF of the test optics. As the latter is typically about one-half of the total PSF, the actual PSF produced by the IFU is about 10–20 per cent better than that indicated in the table (depending on whether a Gaussian or Kolmogorov distribution is used). The effects of diffraction, which become increasingly important as the wavelength increases, have been ignored. The variation of the image quality along the slit is smaller than 5 per cent rms. Further details are given in Paper 3.

The image quality measurements described above were taken at the IFU's nominal output focal surface, which is coincident with the input focal plane. In order to more accurately determine the actual output focus position, we repeated the image quality measurements for the centre slice for various focus positions obtained by translating the output stage along the optical path, but without any adjustments to the input beam simulator.

This indicated that a significant improvement in image quality could be obtained by adjusting the camera focus by ∼0.6 mm to allow $d_{90}$ to be reduced from 0.19 to 0.14 arcsec.

### 6.2 Output pupil

The test equipment was modified to re-image the IFU's output pupil at each position in the field on to a screen placed 2.30-m behind the IFU. The location (centroid) of the output pupil relative to the input pupil (i.e. the projected pupil when the IFU is removed from the optical path), and the size of the (elliptical) output pupil in the spatial and spectral directions, can then be measured, and compared to the nominal location and size. This check has been performed for the full extent of the IFU field, i.e. for a number of points (including the edges) along the length of every slice. It was noted that, when the input beam is moved along the length and width of a single slice, the variation in output pupil location is very small (∼0.3 per cent of the width of the pupil image), so this effect has been ignored.

The measurement results are shown in Fig. 15 for the alignment of the pupil centroids and in Fig. 16 for the pupil dilation. The pupil alignment measurement results show evidence of a (small) aberration in the pupil plane. The alignment errors are ±2.5 mrad in the spatial direction, and ±7 mrad in the spectral direction. The two halves of the slicing mirror array are well aligned causing only a small shift in output pupil location.

To estimate the effect of the misalignment on throughput in the spatial and dispersion case, we modelled the beam as circular and

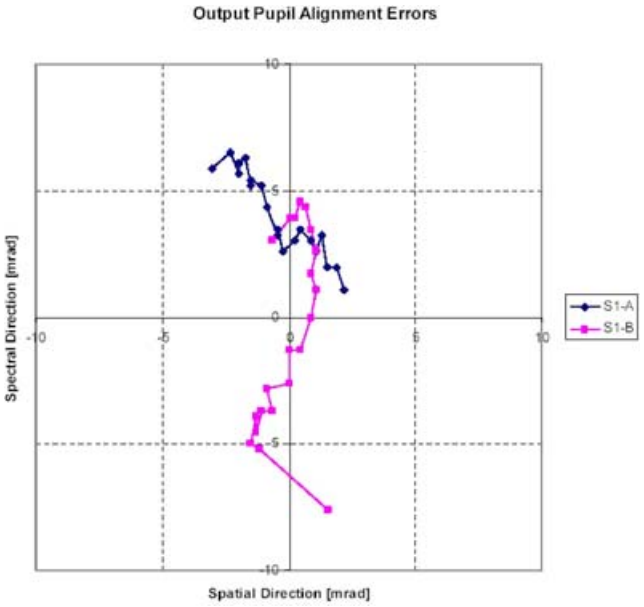


**Figure 15.** Output pupil alignment errors for each optical path.

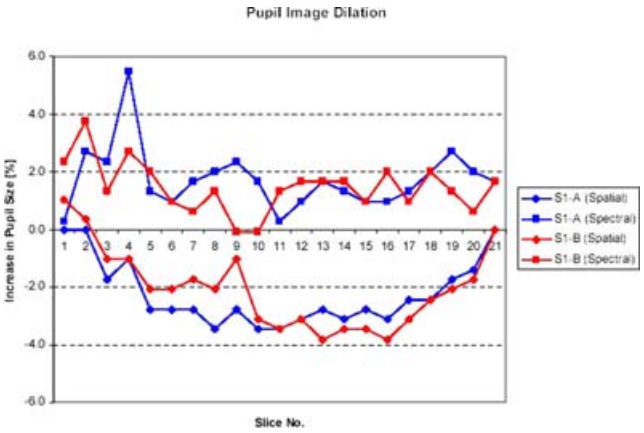


**Figure 16.** Output pupil dilation (size in excess of nominal) for each optical path.

displaced it by 2.5 mrad compared with an f/16 beam and by 7.5 mrad compared to a beam of speed $f/(16 \times 2.3)$. The estimated loss was 5 and 7 per cent, respectively. However, this analysis overestimates the true loss by a large factor because the typical (rms) loss will be ∼3 times smaller; and, in the dispersion direction, the loss will be negligible because the stop is oversized with respect to the anamorphically compressed beam in this direction. The actual loss will depend on the detailed as-built shape of the spectrograph stop, but we expect a loss of ∼2 per cent overall with an rms variation from slice to slice of the same magnitude.

The measurements of the pupil size show that the dilation of the pupil images is very small: less than 2 per cent rms in the spectral direction, whereas the pupil image size actually tends to decrease (by approximately 2.5 per cent rms) in the spatial direction (this is an intended feature of the design – see Paper 3 for further details). The effect of this on throughput is likely to be negligible because of the anamorphic compression of the beam in the spectral direction and the compression of the beam in the spatial direction.

In Paper 2, we present results on the overall throughput which suggest that the effect of pupil misalignment and dilation is indeed very small.

### 6.3 Scattered light and ghosting

The requirement on the intensity of diffuse scattered light produced by the IFU is <50 per cent of the background intensity (assessed in the required wavelength range) due to other sources, e.g. thermal emission from the sky, telescope and GNIRS; detector dark current and readout noise current. Compliance can thus only be verified during commissioning at the telescope. However, we made a basic assessment of the diffuse-scattered light by comparing the background intensity for images of the IFU output PSF with the background intensity for images of the input PSF (i.e. with the IFU removed from the beam). This shows that there is <1 per cent increase in the background intensity caused by the IFU. Whilst this does not demonstrate the IFU's compliance with the specification, it does show that the IFU produces very little diffuse scattered light. These tests were done in the visible but the scattered light should be much less in the infrared.

Although a system consisting only of mirrors should not produce ghost images, we searched for them in any case by systematically moving the input test beam around inside and outside the IFU's field of view, and scanned the output slit for any spurious images. We found no evidence for any ghost images or any other form of spurious illumination (e.g. cross-talk between separate slices). Again, whilst it is not possible to replicate every conceivable configuration of the input field (i.e. location of bright stars which might cause ghost images) in the laboratory, this test suggests that the IFU is indeed not susceptible to the formation of obvious ghost images.

### 6.4 Throughput

Using the test equipment described above, the throughput was measured at optical wavelengths (633 nm) by comparing the intensity of the output beam with that of the reference input beam (i.e. when the IFU is removed from the optical path). The measurement results for slices 3, 11 and 19 are 38, 40 and 36 per cent, respectively ±8 per cent. These are slightly higher than the predictions of the throughput model which gives an average of 33 per cent at 633 nm but agrees within the error bars. This suggests that our throughput model is correct and that the final throughput at 2.5 μm would be ∼90 per cent as predicted (see Paper 2 for verification of this).

### 6.5 Cryogenic tests

A cold test (at a temperature of ∼45 K) was carried out to ensure that the IFU meets its performance requirements under cryogenic conditions. During this test the full complement of system performance parameters was assessed, i.e.: (i) image quality; (ii) throughput; (iii) output pupil alignment and dilation; and (iv) scattered light and ghosting.

The results of the cryogenic test were compared with the results from the baseline tests performed at ambient temperature. No statistically significant difference in the IFU's performance was observed, which demonstrates the IFU's compatibility with the cryogenic environment.

### 6.6 Conclusions of test phase

A comparison of the tolerances and metrology for component geometry and surface form (Tables 3 and 4) reveals a few areas where

the system is out of specification (highlighted in Table 4). However, these are errors relating to complete assemblies which can be (and were) corrected during assembly and alignment of the IFU. It is also important to realize that the tolerance analysis partitions errors between components and degrees of freedom in a way which is not unique. It is therefore possible to violate the component specification is some areas but still produce a system that conforms to the specification. We believe that the system-level tests demonstrate this and the performance on the telescope (Paper 2) shows this to be true. Furthermore some of the measurements presented have significant uncertainty. The error on the radius of curvature, $R$, is $\sigma(R) = -2\ \sigma(h)\ (R/a)^2$ where $a$ is the dimension orthogonal to the normal vector of the surface, $\underline{n}$, where a measurement of the sag is made with uncertainty $\sigma(h)$. The angular error in component $j$ of the normal vector is $\sigma(n_j) = \sigma(h)/a_j$ where $a_j$ is the dimension in that direction. For typical values this implies $\sigma(R) = 0.1$ mm, and a worst-case error in the unit vector direction (for the S2 mirrors) of $\sigma(n_x) = 300\ \mu$ rad. The unit vector uncertainty demonstrates that some of the results in Table 4 are dominated by measurement errors.

The image quality and output pupil definition conform to the specifications comfortably. Although not all of the desired tests could be done at component level, the system-level tests indicate good conformity with the requirements. Although the surface roughness specification was not met, the total throughput measured in the laboratory (and later confirmed on the telescope) is quite acceptable, ranging between 65 and 90 per cent at the extremes of the design wavelength range, compared to the wavelength-independent specification of 70 per cent.

During final assembly, one S3 mirror was damaged, resulting in the effective loss of one-third of slice 13, a region of $1.6 \times 0.15$ arcsec$^2$, amounting to 1.5 per cent of the field. An assessment showed that this damage did not increase the amount of scattered light or produce any other undesirable effect. The risk involved in repairing the damage far outweighed the potential benefit, so no remedial action was taken. This defect should not introduce artefacts into the data if the normal observing techniques used in the near-infrared are used. These involve observing with a pattern of pointings in which the object and background are alternately sampled with a subfield dither pattern for the on-target position to aid the removal of non-uniformities in response over the field and to increase the field size by mosaicking. In this sense, the damage can be viewed as a standard flat-fielding problem.

## 7 CONCLUSIONS AND RELEVANCE TO FUTURE INSTRUMENTATION

We have described the design, component specification and laboratory testing of the GNIRS IFU. This is an innovative system of great relevance to the next generation of telescopes whose instrumentation is largely predicated on highly efficient IFUs of this type.

We show that most of the performance goals have been met with the exception of the surface roughness of the optical components. However, this causes only a small deviation from the throughput specification in the $J$ band while the $K$-band performance is much better than specified. In Paper 2, we will demonstrate the performance on the telescope and verify the astrophysical performance by reference to other data sets. We will also describe the operational characteristics of the instrument and the reduction of the data.

A full assessment of the relevance of this instrument and its innovative aspects (the optical design principle, manufacturing techniques and 'plug-and-play' instrument integration) must wait until the conclusion of Paper 2. Until then, it will suffice to draw attention to the features that make this instrument important to future instrumentation, especially for ELTs whose special requirements are summarized below.

(i) When working in the diffraction-limited regime, the number of spaxels which cover the corrected field of view will be $10^9$–$10^{11}$ which implies the need to dilutely sample the field via deployable pickoff units which relay selected portions of the field to a spectrograph or imager.

(ii) IFS is the most efficient and accurate method for obtaining spectral information from a small field. In the diffraction limit, it is obvious that the spatial information contained in each subfield should be preserved. Problems of photon starvation due to the fine subdivision of the spatial domain when not at the diffraction limit are much reduced by the large aperture of the telescope.

(iii) The application of such multiple-field concepts implies a high degree of duplication and modularization of the optical trains comprising the spectrograph and any reformatting unit such as an IFU. Each optical train should be essentially identical to reduce costs. Small size and optical adaptability are major advantages.

As we have already noted, Image slicing is the most efficient IFS technique in terms of specific information density. This is because complete slices of the sky are reformatted on the detector. Thus only the small portion of the detector, between adjacent slices, needs to be masked off to prevent cross-talk between unrelated parts of the sky. In contrast, lenslet arrays must leave gaps between each spatial sample in the 2D sampling array defined by the lenslets. As demonstrated in Section 3.1, fibre-lenslet arrays must, in practice, use several detector pixels to sample each spatial resolution element defined by the aperture of the fibres or their coupling lenslets. With a slicer, only one detector pixel is required for each spatial sample in the direction perpendicular to dispersion. Diffraction losses are also reduced since the field is sampled in one dimension only compared to the two of the other techniques.

The AIS has the further advantage over earlier image slicer designs that it produces a real pseudo-slit making it straightforward to interface to beam-fed spectrographs, and requires less extreme ray angles due to its careful control of pupil imagery which leads to fewer aberrations and therefore better image quality and/or smaller size and cost. Furthermore the use of anamorphism allows for the sampling element to be the same size in both dimensions, whilst simultaneously providing critical sampling in the spectral direction and also reducing diffraction losses compared to a conventional slit with the same projected width.

From the preceding paragraphs, it can be seen that: (i) IFS is a vital technique for ELTs; (ii) multiple IFS will be required to exploit them, making use of massively parallel optical systems and (iii) the AIS principle gives the highest potential performance of any IFS system and is the most amenable to the miniaturization implicit in the parallelism requirement.

The disadvantages of this approach are: (i) the complexity of the optical system and the numbers of tiny mirror facets required; (ii) current limitations on surface roughness which preclude efficient use in the visible and (iii) that the IFU does not incorporate a naturally flexible coupling as does a fibre-based system. These issues are being addressed by the CfAI and other groups. These include: (i) the provision of a facility, dedicated to astronomy, for the manufacture of the optics by diamond machining; (ii) experimentation with post-machining surface processing to improve surface quality and the use of alternative materials such as ceramics to improve surface finish and (iii) the design of stable articulated pickoff arms that transfer the subfield to a fixed IFU while preserving the optical path

length. Many of these improvements are being realized for KMOS (Sharples et al. 2004) which is a multi-IFS near-infrared instrument for the VLTs. Preliminary results indicate that surface roughness of 10-nm rms is achievable by direct machining of aluminium alloys and that a further improvement of a factor of 2 is achievable by surface processing (Schmoll et al. 2006). This three- to four-fold improvement in roughness over that obtained with the GNIRS IFU implies IFU throughputs of ∼70 per cent at wavelength 0.5 μm, limited by the coating reflectivity rather than the roughness of the surfaces (see Paper 2).

## ACKNOWLEDGMENTS

We thank Colin Dunlop, Gil Moretto and Sergei Pokrovski for their contribution to the optical testing of the IFU. We also thank the GNIRS team for their excellent instrument and help with our work. We also thank the Gemini project for supporting this work through thick and thin (especially Doug Simons, Fred Gillett and Matt Mountain) and the staff who worked with us at the telescope especially: James Turner and Bernadette Rogers.

The Gemini Observatory is operated by the Association of Universities for Research in Astronomy, Inc., under a cooperative agreement with the NSF on behalf of the Gemini partnership: the National Science Foundation (United States), the Particle Physics and Astronomy Research Council (United Kingdom), the National Research Council (Canada), CONICYT (Chile), the Australian Research Council (Australia), CNPq (Brazil) and CONICET (Argentina).

## REFERENCES

Allington-Smith J. R., 2006, New Astron. Rev., 50, 244
Allington-Smith J., Content R., 1998, PASP, 110, 1216
Allington-Smith J. et al., 2002, PASP, 114, 892
Bacon R. et al., 2001, MNRAS 326, 23
Bower R. G. et al., 2004, MNRAS, 351, 63
Content R., 1997, Proc. SPIE, 2871, 1295
Dubbeldam C. M., Robertson D. J., Preuss W., 2004, SPIE, 5494, 163
Eisenhauer F. et al., 2004, AN, 325, 120
Larkin J. et al., 2006, New Astron. Rev., 50, 362
LeFevre O. et al., 2003, Proc. SPIE, 4841, 1670
Gerssen J., Allington-Smith J., Miller B. W., Turner J. E. H., Walker A., 2006, MNRAS, 365, 29
Pasquini L. et al., 2000, SPIE, 4008, 129
Schmoll J. C. M., Dubbeldam C. M., Robertson, D. J., Yao, J., 2006, New Astron. Rev., 50, 337
Sharples R. M. et al., 2004, Proc. SPIE, 5492, 1179
Weitzel L., Krabbe A., Kroker H., Thatte N., Tacconi-Garman L. E., Cameron M., Genzel R., 1996, A&AS, 119, 531

This paper has been typeset from a TEX/LATEX file prepared by the author.